Dry reforming of methane in an atmospheric pressure glow discharge : confining the plasma to expand the performance

Dry reforming of methane in an atmospheric pressure glow discharge: confining the plasma to expand the performance

Bart Wanten, Stein Maerivoet, Christine Vantomme, Joachim Slaets, Georgi Trenchev, Annemie Bogaerts

Research group PLASMANT, University of Antwerp, Department of Chemistry, Universiteitsplein 1, B-2610 Antwerp, Belgium

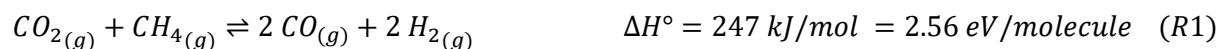E-mail: bart.wanten@uantwerpen.be; annemie.bogaerts@uantwerpen.be

Abstract

We present a confined atmospheric pressure glow discharge plasma reactor, with very good performance towards dry reforming of methane, i.e., CO_2 and CH_4 conversion of 64 % and 94 %, respectively, at an energy cost of 3.5 - 4 eV/molecule (or 14 – 16 kJ/L). This excellent performance is among the best reported up to now for all types of plasma reactors in literature, and is due to the confinement of the plasma, which maximizes the fraction of gas passing through the active plasma region. The main product formed is syngas, with H_2O and C_2H_2 as by-products. We developed a quasi-1D chemical kinetics model, showing good agreement with the experimental results, which provides a thorough insight in the reaction pathways underlying the conversion of CO_2 and CH_4 and the formation of the different products.

Keywords
Plasma; dry reforming of methane; atmospheric pressure glow discharge; syngas formation; chemical kinetics modelling

1. Introduction

CO_2 and CH_4 are the two main greenhouse gasses, so their conversion into valuable products is one of the most important subjects in current catalysis, energy and environmental research.[1] By means of dry reforming of methane (DRM, (R1)), CO_2 and CH_4 are converted into syngas (CO and H_2):

$$CO_{2(g)} + CH_{4(g)} \rightleftharpoons 2\ CO_{(g)} + 2\ H_{2(g)} \qquad \Delta H° = 247\ kJ/mol\ = 2.56\ eV/molecule \quad (R1)$$

Syngas can be used as building block for several value-added chemicals, including methanol and long-chain hydrocarbons through the Fischer-Tropsch process.[1–4] DRM is seen as an attractive alternative for the steam reforming of methane (SRM), as the latter generally produces syngas with a H_2/CO ratio of 3, which is much higher than needed for the synthesis of these value-added chemicals.[1–4] In addition, SRM leads to a net CO_2 production, while DRM allows for a net CO_2 conversion. Therefore, a lot of research has been and is being performed on DRM, due to its large potential as future process to produce syngas in a much more sustainable way. However, reaction (R1) is highly endothermic, so it must be carried out at high temperatures. In addition, classical DRM suffers from catalyst deactivation, and so far this has severely limited its potential. This explains why DRM is not yet being applied on a large scale.[1–3]

Plasma technology provides an alternative route for DRM.[5] A plasma is an ionized gas, created by applying a large potential difference between two electrodes between which the gas flows. Because electrons are selectively heated by the electric field, they can activate the gas molecules and a very

reactive mixture arises, containing radicals, ions and excited species. Hence, the gas should not be heated as a whole to induce endothermic chemical reactions, making plasma-chemical conversion potentially more energy-efficient than classical thermal conversion. Furthermore, the process only requires electricity and it can be turned on and off fast, so it can easily handle the intermittent character of renewable energy sources.[5,6]

The performance of several types of plasma reactors for DRM has been tested in recent decades.[5,6] Despite the promising results, many plasma reactors still suffer from limitations. On one hand, the conversion is sometimes limited because a large fraction of the feed gas does not pass the plasma, like is the case for most gliding arc (GA) plasma reactors[5,7,8]. On the other hand, the energy cost is often too high, which is a common problem for dielectric barrier discharges (DBD).[5,9–11] Snoeckx and Bogaerts[5] defined a maximum energy cost of 4.27 eV/molecule as target for plasma technology to be competitive with classical DRM and other emerging technologies. They presented a comprehensive overview of the performance for all types of plasma reactors described in literature, and demonstrated that most plasma types cannot yet reach this target. According to that overview, only a spark discharge[12] and especially an atmospheric pressure glow discharge (APGD)[13] were able to combine energy costs below this target with relatively high conversions (see section 3.3 for further discussion).

Glow discharges can be distinguished from other plasmas by their specific voltage-current characteristics: they typically combine a low current (a few to a few tens of mA) with a high voltage (a few to a few tens of kV).[14] Furthermore, they display a different discharge structure compared to other DC plasma sources, i.e. gliding arc. The tendency towards field emission in a glow discharge, rather than thermionic cathode emission (arc discharge) is most prominent. While APGDs appear very promising for DRM, they have not been studied to a large extent[5,13,15–17]. In addition, the exceptionally good results for the APGD presented by Li et al.[13] raise some questions with respect to the low powers that were measured (and which lead to very low energy costs). In other words, the performance of APGD reactors towards dry reforming of methane is not fully clear, and requires further investigation.

The performance of APGDs towards CO_2 splitting, in three different designs, was recently investigated by Trenchev et al.[14] The authors showed a clear improvement in terms of CO_2 conversion in a so-called confined APGD, which ensures encapsulation of the plasma zone by a high-temperature resistant ceramic material, maximizing the fraction of gas that is activated by the plasma. This new design has not been tested yet for DRM.

Therefore, in this paper, we study the performance of a confined APGD towards DRM to investigate its potential, with respect to the current state-of-the-art. We performed experiments for a wide range of currents, flow rates and CO_2/CH_4 ratios. In addition, we developed a chemical kinetics model, to explain the experimental trends. In this way, we do not only obtain more insight in the reactor's current potential, but we are also able to understand the underlying chemistry and highlight limitations of our current approach, enabling us to already pinpoint further improvements.

2. Experiments and Modelling

2.1. Description of the experimental set-up

The APGD plasma reactor under study (Figure 1) consists of a cathode pin and anode plate, both made from stainless steel (Therma 310S). The cathode and the discharge region are fully surrounded by a tube made of Macor® machinable high temperature ceramic, with an inner radius of 2.5 mm. The cathode contains a groove of ± 1 mm deep, through which the gas can enter the discharge zone. This provides a high gas velocity close to the cathode, to effectively cool the latter. The anode plate is

positioned at the end of the ceramic tube, at a distance of 22 mm from the cathode tip, and contains an opening in the centre through which the gas can exit the reactor.
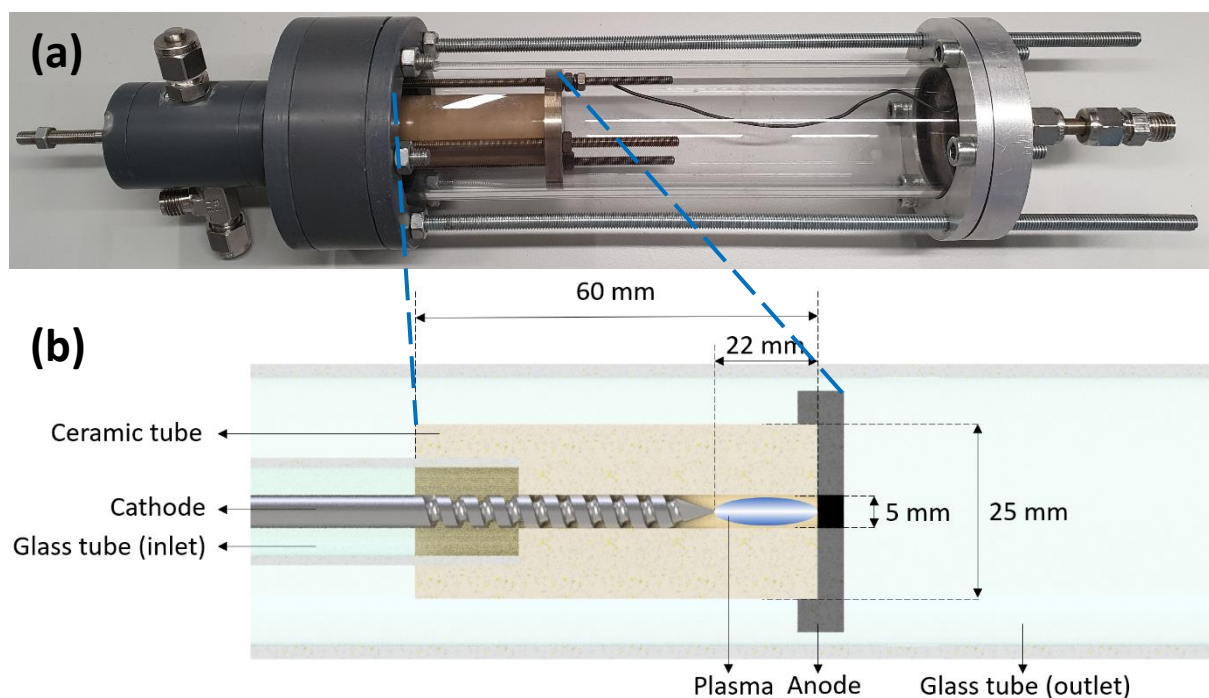
Figure 1: Photograph (a) of the confined APGD plasma reactor and schematic representation (b) with important parts and dimensions indicated.

The entire experimental set-up is presented in Figure 2. A high voltage Technix DC power supply capable of supplying up to 30 kV and 40 mA is used to deliver the power to the plasma. The plasma is sustained in the glow regime by means of a 300 kΩ ballast resistor. The initial voltage has been pre-set each time to 30 kV, after which it drops once the plasma is ignited to a value that can be read directly from the power supply (around 10-15 kV, depending on the applied conditions). The flow rate of all feed gasses is regulated by Bronkhorst mass flow controllers.

The gas mixture flowing out of the reactor first goes through a liquid trap to remove any liquid products, and the remaining gas mixture is analysed by means of a Thermo Scientific Trace 1310 Gas Chromatograph (GC). For every condition, a blank measurement is performed next to three plasma measurements. N_2 is used as internal standard to account for the effects of gas expansion and of condensation of liquid products on the measured concentrations, and is added to the gas mixture after the reactor. The weighted averages of the CO_2, CH_4 and total conversions are calculated, as well as the product selectivities and yields, based on the measured concentrations. The energy costs are calculated based on the total conversions and specific energy input (SEI), which is defined as the ratio of plasma power over total gas flow rate. Finally, the concentration, selectivity and yield of the collected liquid fraction is estimated based on a procedure described by Pinhão et al.[18] More details on the experimental analysis is presented in the supporting information (SI; section 1).
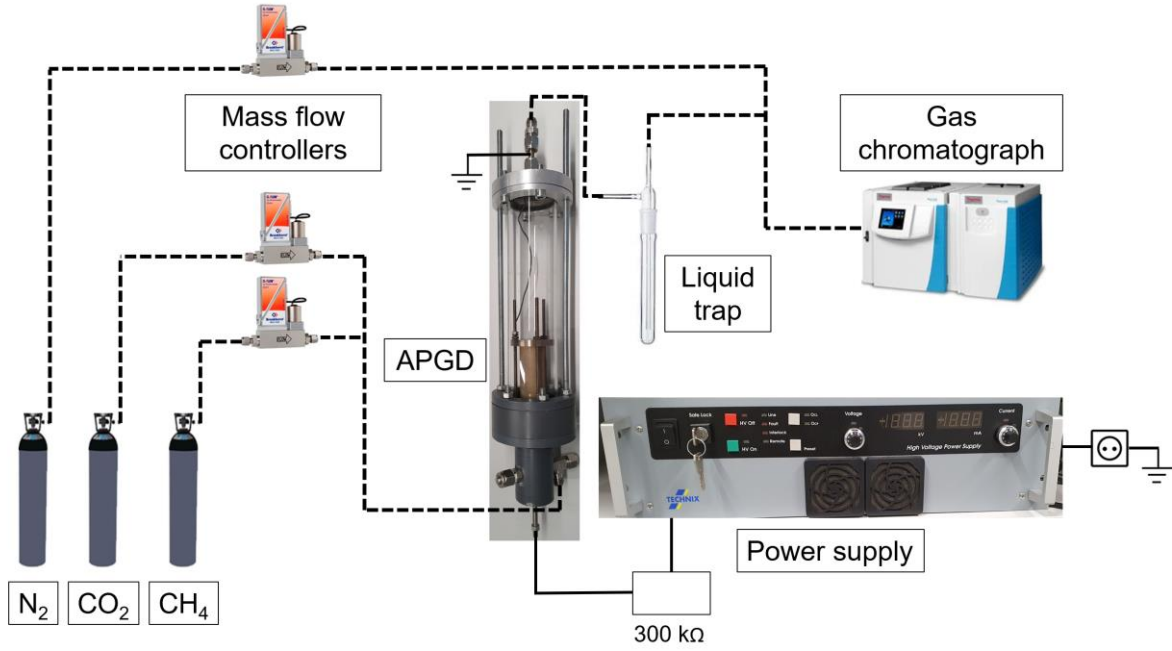
Figure 2: Schematic overview of the experimental set-up. Electrical connections are represented by full lines, gas connections by dashed lines.

2.2. Description of the chemical kinetics model

In order to obtain insight in the underlying chemistry, we developed a quasi-one dimensional (quasi-1D) chemical kinetics model, to describe the plasma chemistry, by means of the Zero-Dimensional Plasma Kinetics (ZDPlasKin) solver[19]. The latter is a Fortran 90 module which, for all species taken into account in the chemistry set, solves the mass conservation equation by means of production and loss rates, defined by the chemical reactions:

$$\frac{dn_s}{dt} = \sum_r \left[(a_{sr}^R - a_{sr}^L)k_r \prod_l n_l^L \right] \tag{E1}$$

In equation (E1), n_s stands for the density of species s (in m^{-3}), a_{sr}^R and a_{sr}^L are the stoichiometric coefficients of species s at the left and right side of reaction r, respectively. n_l is the density of species l on the left side of the reaction and k_r is the reaction rate coefficient of reaction r. The rate coefficients for heavy particles are derived from literature[20], as a constant or as a function of gas temperature. The rate coefficients for electron impact reactions depend on the electron energy distribution function (EEDF), and the latter is derived from the Boltzmann equation, solved by the BOLSIG+ solver[21], included in the ZDPlasKin code. Equation (E1) is solved each time step with the updated species densities and rate coefficients from the previous time step, for all reactions included in the chemistry set. In this way a loop is created, and the species densities at any specific time step can be determined. More details on the formulas and a flow chart of the simulation process, can be found in the SI (section 2.1 and 2.2). In addition, we also present there the calculated electron density, reduced electric field and electron temperature as a function of position, because these are important plasma parameters, which give more information on the parameter range in which our reactor is operating.

123 species are included in the chemistry set, including various ground-state molecules, excited species, ions and radicals, as well as the electrons (see Table 1). Furthermore, 6849 reactions are included, consisting of vibrational-translational (VT) and vibrational-vibrational (VV) relaxation

reactions, electron impact reactions, neutral-neutral, ion-neutral, ion-ion and electron-ion (recombination) reactions. A list of the reactions with their corresponding reaction rate constants can be found in Heijkers[22]. More information on the vibrational (V) and electronic (E) excited states is presented in the SI (section 2.3).

Table 1: Overview of all species included in the chemistry set of the quasi-1D model.

Neutral molecules	Charged species	Radicals	Excited molecules
	H^+, H_3^+, e^-	H	
CO_2	CO_2^+		$CO_2(V_{A-D})$, $CO_2(V_{1-21})$, $CO_2(E_1)$
CO	CO^+, CO_3^-, CO_4^-		$CO(V_{1-10})$, $CO(E_{1-4})$
O_2	O^-, O^{2-}	O	$O_2(V_{1-4})$, $O_2(E_{1,2})$
CH_4	CH_5^+, CH_4^+, CH_3^+, CH_2^+, CH^+	CH_3, CH_2, CH	
H_2	H_2^+		$H_2(V_{1-14})$
C_3H_8, C_3H_6, C_2H_6, C_2H_4, C_2H_2	$C_2H_6^+$, $C_2H_5^+$, $C_2H_4^+$, $C_2H_3^+$, $C_2H_2^+$, C_2H^+	C_3H_7, C_3H_5, C_2H_5, C_2H_3, C_2H, C	
H_2O, H_2O_2	H_2O^+, H_3O^+, OH^-, OH^+	HO_2, OH	
CH_2O, CH_2CO, CH_3OH, CH_3CHO, CH_3OOH		CHO, CH_2OH, CH_2CHO, CH_3O, CH_3CO, C_2HO, CH_3O_2	

ZDPlasKin calculates all plasma properties only as a function of time. In other words, processes like diffusion or convection are not included. However, we can translate the time-dependence into a spatial dependence by assuming a constant velocity in the axial direction. This is possible due to the similarity between a batch reactor (where the composition is considered uniform, hence 0D, but changes as a function of time) and a plug flow reactor (where the composition changes as a function of axial position in the same way, and where the residence time, defined by the flow rate or velocity, is the same as in the batch reactor). Our APGD plasma reactor can indeed be approximated as a plug flow reactor. A schematic representation of this concept is given in the SI (section 2.4). Therefore, while we do not take processes like diffusion into account directly, information on the species densities as a function of position in the plasma can be obtained. Hence, the model can be considered to be a quasi-1D model.

Next to the chemistry set, we also used a velocity and temperature profile in the reactor as input for the model. A 3D turbulent flow model with the exact geometry of the reactor was designed in COMSOL Multiphysics®, to derive the average axial flow velocity for each simulated region. In addition the order of magnitude of the temperature was based on fluid dynamics simulations performed for an APGD reactor operating in CO_2[14]. Indeed, deriving the temperature profile in the plasma reactor is quite a challenge, especially in case of dry reforming of methane where we would have to include a rather extensive chemistry set. However, since in our experiments the CH_4 fraction does not exceed 35%, we believe that the resulting temperature range predicted by the model from Trenchev et al.[14] is a reasonable explanation for our CO_2-CH_4 mixtures. More details are given in the SI (section 2.5).

Additionally, the formulas to calculate the concentrations and gas expansion factor based on the simulated species densities, are presented in the SI (section 2.6).

3. Results and discussion

First we present the obtained conversions and energy costs as a function of electrical current, gas flow rate and CH_4 fraction in the mixture. Simultaneously, we compare the experimental results with the simulated values from the model, for exactly the same conditions. Subsequently, we compare our results with the current state-of-the-art on plasma-based DRM. Next, we analyse the product output in terms of syngas ratio, selectivity and yield for the various conditions, again compared with the simulated results to validate our quasi-1D model. Finally, we present a reaction pathway analysis, to obtain a better understanding of the underlying chemistry.

3.1. Conversion

The conversion of reactant i (either CO_2 or CH_4) is defined in equation (E2):

$$X_i = \frac{c_i^{in} - \alpha \cdot c_i^{out}}{c_i^{in}} = 1 - \frac{\alpha \cdot c_i^{out}}{c_i^{in}} \qquad (E2)$$

With c_i^{in} and c_i^{out} the concentration of i at the in- and outlet of the reactor, respectively. A correction factor α is determined based on the signal of the internal standard at a blank and plasma measurement, and is used to correct for changes in concentration with a plasma measurement, due to gas expansion inherent to DRM (see (R1)), and due to the condensation of liquid products, as explained in detail in the SI (section 1.2).

The total conversion is the weighted average of the conversion of each reactant over their concentration in the inlet gas mixture:

$$X^{tot} = \sum_i c_i^{in} \cdot X_i \qquad (E3)$$

The CO_2, CH_4 and total conversion are presented in Figure 3, for different currents (a) and flow rates (b), at a CH_4 fraction of 25%, as well as for different CH_4 fractions, at 35 mA & 1 L/min (c), and at 25 mA & 0.5 L/min (d).
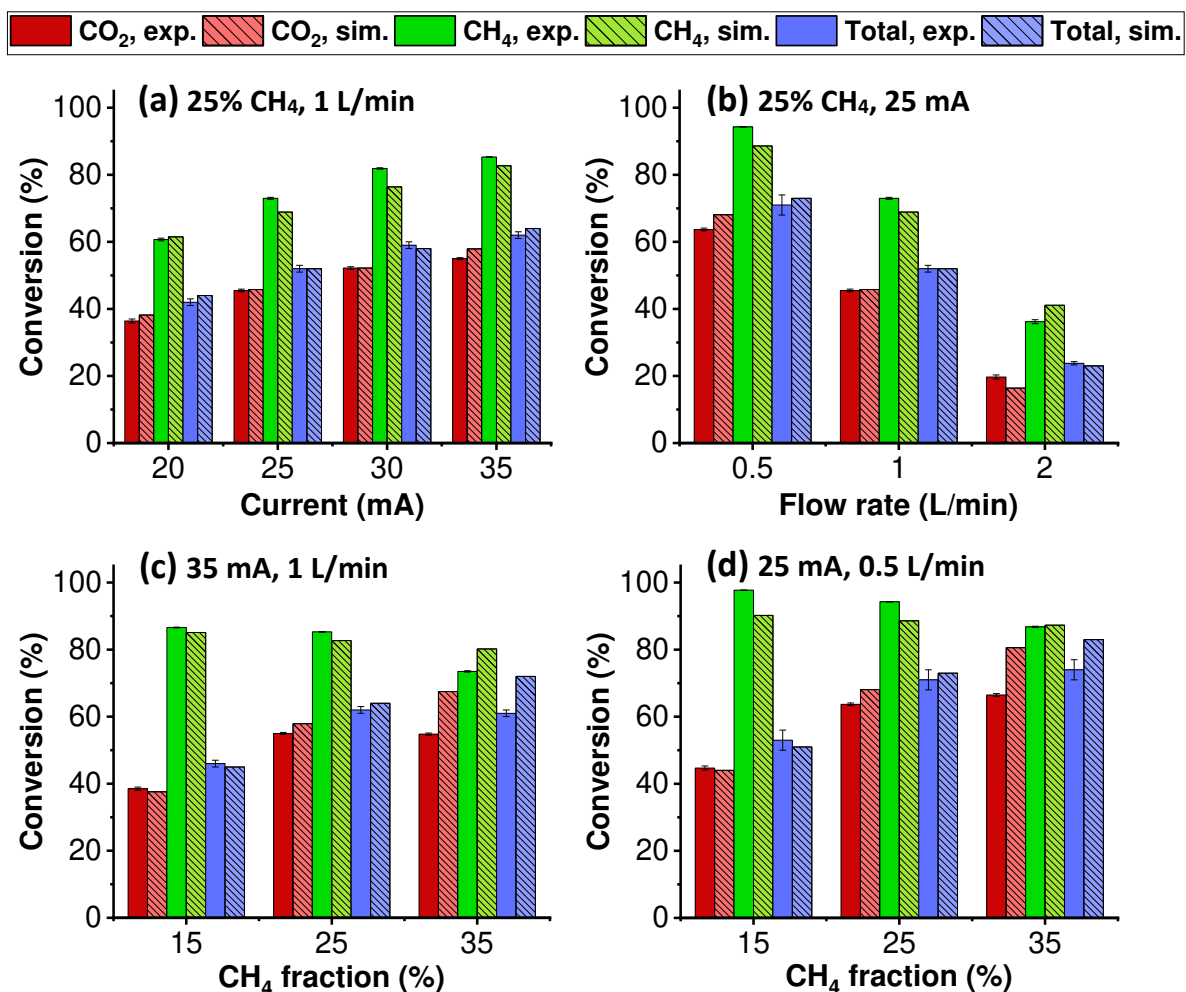
Figure 3: Experimental and simulated CO_2 and CH_4 conversion, as well as total conversion, for different currents (a), flow rates (b) and CH_4 fractions (c, d). The other conditions (CH_4 fraction, current, flow rate) that are kept constant, are indicated in the figure. Error bars are added for the experimental results, but are often too small to be visible.

It is clear that the CH_4 conversion is much higher than the CO_2 conversion, which makes sense, as the bond breaking energy for a C-H bond (4.48 eV) is much lower than for a C=O bond (5.52 eV).[5,7] Furthermore, a higher current or lower flow rate yields a higher conversion, due to a higher SEI (= ratio of plasma power over flow rate). Higher currents or lower flow rates than shown here unfortunately resulted in overheating and damage of some reactor parts, like the ceramic tube, cathode and resistor.

In addition, upon rising the CH_4 fraction in the mixture, the CO_2 conversion clearly rises, while the CH_4 conversion slightly drops. As a result, the total conversion increases significantly from 15 to 25% CH_4, but remains more or less constant upon further increasing to 35% CH_4. The latter is attributed to two aspects: the drop in CH_4 conversion, which affects the total conversion the most at 35% CH_4, and because of significant carbon formation, affecting the plasma stability. Indeed, upon increasing the CH_4 fraction, the plasma became increasingly unstable, leading to a clear negative effect on the conversion and the reactor's performance in general. For this reason, we did not perform experiments at CH_4 fractions higher than 35%. The rising trend in CO_2 conversion and decreasing trend in CH_4 conversion are a consequence of changes in the plasma chemistry, which will be discussed in section 3.5.

The above trends as a function of current (or power), flow rate and gas mixing ratio correspond well with other reports in literature[5]. More important, however, is the level of conversion that is reached here. For instance, at 0.5 L/min, 25 mA and 25% CH_4, the CO_2 and CH_4 conversion reach 63.7 ± 0.4 %

and 94.28 ± 0.07 %, respectively, leading to a total conversion of 71 ± 3 %. These values are higher than what is typically reported in literature for plasma-based DRM[5] (see also section 3.3 below), which is obviously due to the large gas fraction passing through the plasma, i.e. a direct effect of confining the glow discharge by the ceramic tube.[14] Indeed, earlier plasma fluid dynamics simulations revealed that the glow discharge plasma exhibits a width of approximately 4 mm, and does not fill the entire reactor if the latter is much wider, which was the case for the basic APGD reactor, studied by Trenchev et al.[14] The same issue also occurs in typical GA plasmas, where the plasma arc is located in the centre, and a large fraction of gas passes through the reactor without being converted, as reported in literature multiple times.[7,8,23–25] Hence, by inserting a ceramic tube with an inner diameter comparable to the plasma width, we ensure that the plasma fills most of the reactor, and the fraction of gas passing through the active plasma region is maximized. Whether this is the only effect that leads to these high conversions, is not 100% certain, as the ceramic tube could also facilitate a certain "wall stabilization" effect.[26] Due to the direct contact of the plasma with the ceramic walls, the temperature gradient of the discharge in the radial direction is flattened, i.e. the plasma itself is additionally cooled, while the surrounding gas is additionally heated. This leads to lesser contraction of the plasma (i.e., the plasma stabilizes or "sticks" to the constricting walls), leading to a larger zone where the conditions for CO_2 and CH_4 conversion are fulfilled, in contrast to a non-confined set up. The full effect of wall-stabilized plasmas in general is still under investigation[27], but regardless, as was proven by Trenchev et al.[14], confinement of the plasma certainly causes an increase in conversion.

In general, a good agreement is reached between model and experiments, for all conditions, both in absolute values and in trends. Only at 35% CH_4, there is a larger discrepancy, probably because of the plasma instability due to carbon formation, and this instability cannot be accounted for in the model. Nevertheless, based on the overall satisfactory agreement, certainly keeping in mind the approximations inherent to the quasi-1D model, we can use the model to explain the experimental trends from a chemical point of view. Note that the latter is not possible in case of a purely experimental study, which lacks detailed insight in the underlying chemistry. While a model is always an approximation of the reality, we believe our model provides a realistic picture because all assumptions are based on logical and plausible physics, and it uses a very extensive chemistry set, leading to a satisfying agreement between our model and the experiments. This combined experimental-modelling approach is one of the novel aspects of our paper, next to the novel design of the confined APGD reactor, which is used for the first time for DRM.
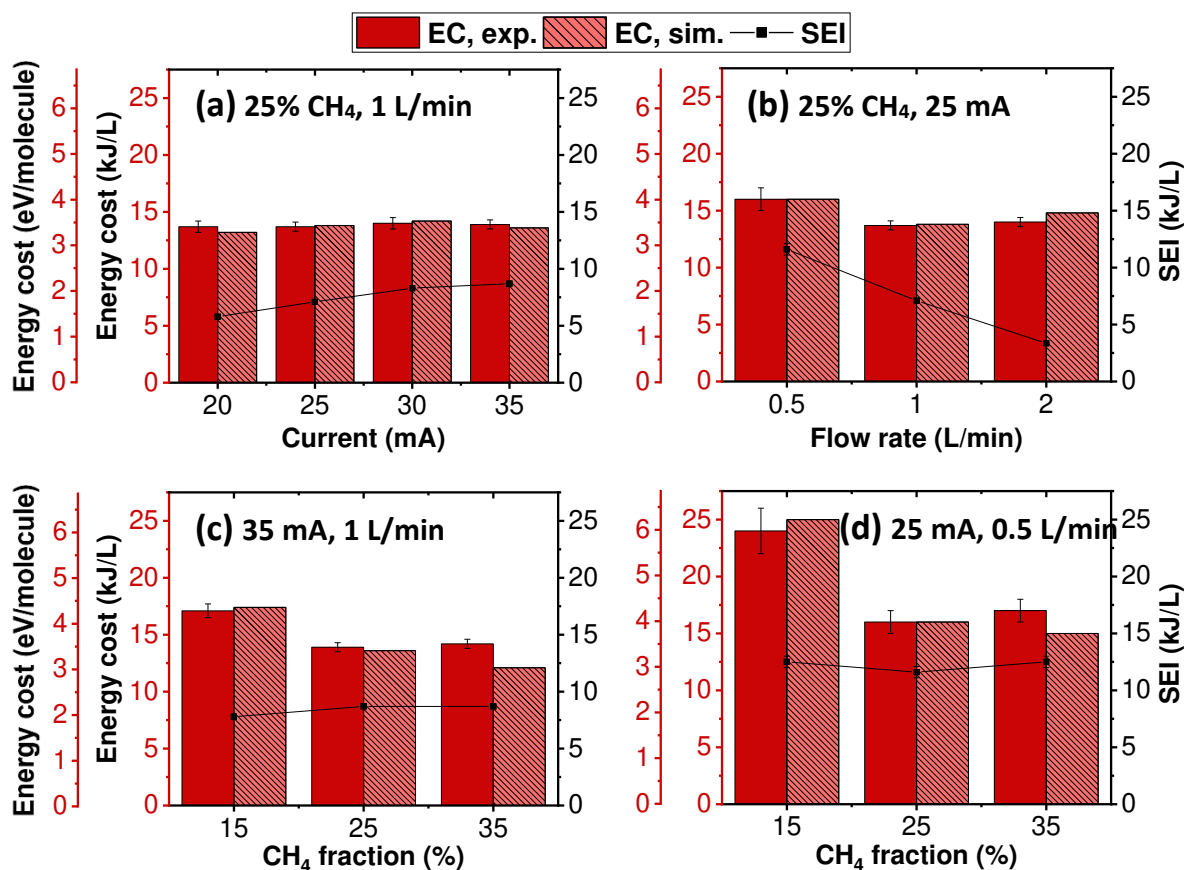
3.2. Energy cost

The energy cost (in kJ/L or eV/molecule) is calculated from the total conversion and SEI, as described in equation (E4) and (E5):

$$EC\left(\frac{kJ}{L}\right) = \frac{SEI\left(\frac{kJ}{L}\right)}{X^{tot}} \tag{E4}$$

$$EC\left(\frac{eV}{molecule}\right) = \frac{SEI\left(\frac{kJ}{L}\right)}{X^{tot}} \cdot \frac{V_{mol}\left(\frac{L}{mol}\right) \cdot \frac{6.24 \cdot 10^{21} eV}{kJ}}{\frac{6.02 \cdot 10^{23} molecules}{mol}} \tag{E5}$$

With V_{mol} equal to 24.05 L/mol at normal conditions. Figure 4 presents the measured and simulated energy cost, as a function of current (a), flow rate (b), both again for 25% CH_4, and as a function of CH_4 fraction, for 35 mA & 1 L/min (c) and 25 mA & 0.5 L/min (d). We also plot the SEI in Figure 4 (black curves, right y-axis). Since we used the experimental SEI as input in our model, the agreement between experiments and model towards energy cost is the same as for the conversion.

Figure 4: Experimental and simulated energy cost as a function of current (a), flow rate (b) and CH$_4$ fraction (c, d). The other conditions that are kept constant are indicated in the figure. Error bars are added for the experimental results, but are often too small to be visible. The energy cost is calculated from the total conversion and SEI, and therefore, the latter is also plotted for all conditions (black curves, right y-axis).

The energy cost is typically in the order of 13-16 kJ/L, or 3.2-4 eV/molecule, for all conditions investigated (except at a 15% CH$_4$ fraction, where it is a bit higher). Indeed, it remains overall constant as a function of current, and varying the flow rate also has no significant effect (certainly not between 1 and 2 L/min), which indicates that the rise in conversion (upon higher current and lower flow rate) is proportional to the rise in SEI (see equation (E4) or (E5)). Note that in literature often a higher energy cost is observed for a higher SEI, because the conversion often levels off upon rising SEI.[5] This shows another advantage of the confined APGD plasma reactor: because a high level of conversion can be reached for DRM, it allows for a proportional rise in conversion with respect to the SEI, at least up to a certain level. Indeed, for 0.5 L/min the energy cost is slightly higher, probably due to more heat loss towards the walls of the ceramic tube. Of course, when confining the plasma, heat losses to the walls are unavoidable, but we use a material that is relatively non-conductive towards heat, so that most of the energy is still kept inside the discharge zone.

The SEI stays almost constant for different CH$_4$ fractions, so when comparing the energy cost for the different CH$_4$ fractions, we observe the opposite trend as for the total conversion. This is logical, and can be deduced from equation (E4), because the energy cost is inversely proportional to the total conversion. Indeed, the energy cost drops upon increasing the CH$_4$ fraction from 15 to 25%, while it stays more or less constant from 25 to 35%.

3.3. Comparison with state-of-the-art

We can conclude that our best results are obtained at 35% CH$_4$, 25 mA and 0.5 L/min (highest total conversion, i.e., 74 ± 3 %, with an energy cost of 17 ± 1 kJ/L or 4.2 ± 0.2 eV/molecule) and at 25% CH$_4$,

35 mA and 1 L/min (lowest energy cost of 13.9 ± 0.4 kJ/L or 3.5 ± 0.1 eV/molecule, for still a relatively high total conversion of 62 ± 1 %). These are among the best results reported up to now for plasma-based DRM. Indeed, Snoeckx and Bogaerts[5] provided a very extensive literature overview of the state-of-the-art in 2017, illustrating the energy cost vs total conversion for DRM in all types of plasma reactors reported in literature. We have updated this overview with additional data points, based on more recent literature[8,28–37]: see Figure 5.

It should be noted that the effects of gas expansion are not described in detail in every paper included in this overview, and this can lead to largely overestimated values towards conversion if not properly taken into account[18]. Nevertheless, we consider that this is always done correctly.
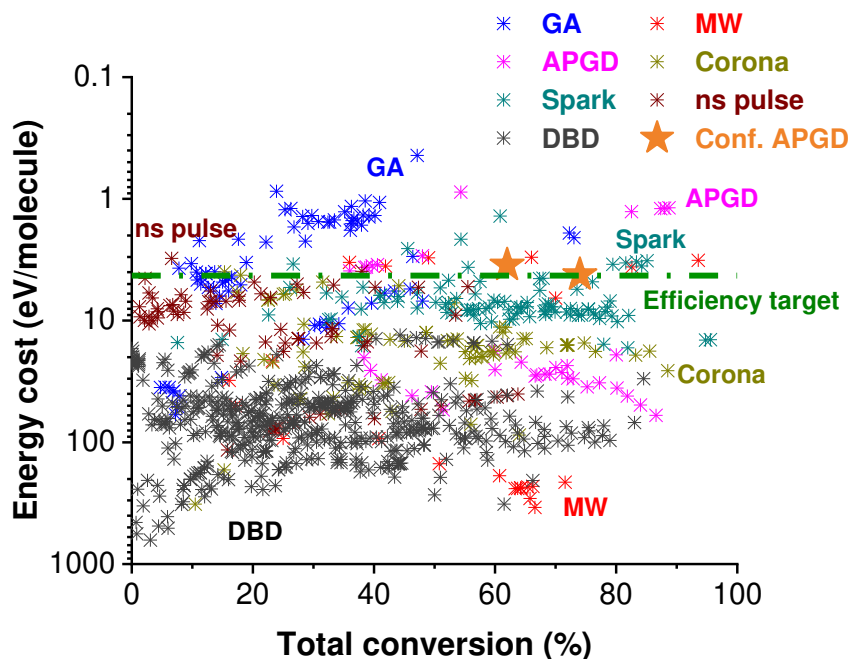
Figure 5: Overview of energy cost vs total conversion, for a large number of different plasma reactors, collected from literature by Snoeckx and Bogaerts[5], updated by us with additional data points, based on more recent literature[8,28–37]. Note that the y-axis is reversed. The efficiency target is defined as the energy cost which should be reached in order to be competitive with classical DRM and other emerging technologies for producing syngas. Our own best results (at 25% CH_4, 35 mA & 1 L/min and 35% CH_4, 25 mA & 0.5 L/min) are added as orange stars.

The best results obtained with our confined APGD are added as orange stars to this overview (see upper right corner). As we can see, our own results reach a fairly high conversion, at an energy cost better than the efficiency target determined by Snoeckx and Bogaerts[5] (see Introduction). The main reason for these good results is the confinement of the plasma by the ceramic tube. It was already demonstrated for CO_2-splitting that this confinement leads to a significant improvement in conversion[14], and our results confirm that the same is true for DRM. Results from many GA reactors stay well below our best results in terms of the combination of total conversion and energy cost, as confining the plasma is less straightforward for such plasma types, due to the high temperatures at these lower flow rates.[5,7,8,23–25]

There are however a few data points, although originating from only five papers, with still a higher conversion and a lower energy cost combined[12,13,29,33,35]. A spark discharge[12] and especially another APGD set-up[13] were already mentioned in the introduction, and by updating the overview with more recent literature data, a GA set-up[29] and two microwave (MW) plasma reactors[33,35] also appear to lead to better results. However, the better results with the spark discharge from Chung et al.[12] and the GA from Li et al.[29] were obtained in combination with catalysts, which typically leads to a higher

conversion. Additionally, Li et al.[29] added a small fraction of O_2 to increase the conversion. The combination with catalysts, as well as the addition of other gasses like O_2, has not been tested yet with our APGD and is planned for future work, but it may be expected to lead to better results as well.

As for the other APGD set-up from Li et al.[13], we have some concerns about the correct measurement of power (because the voltage drop differs from the expected behaviour), and obviously this power determines the SEI, and hence the energy cost. Finally, the MW plasma reactors from Sun et al.[33] and Chun et al.[35] also result in a better combination of conversion and energy cost, attributed to the reactor design and/or plasma characteristics. Nevertheless, it is clear that our confined APGD plasma reactor is very promising for DRM, also due to its very simple, inexpensive design and easy operation.

3.4. Product output

As stated in the Introduction, the goal of DRM is to produce syngas, which can be further converted into methanol, or other valuable chemicals such as olefins and hydrocarbons in the Fischer-Tropsch process.[3,5] Summarized, the ideal H_2/CO or syngas ratio is close to 1 when targeting aldehydes, 2 when targeting alcohols and olefines, and a (2n+1/n) ratio when targeting paraffins.[2,38] Currently, syngas is mainly provided through SRM, which results in a H_2/CO ratio of 3, which is higher than required.[2,3,29,37] Therefore, it is important to assess the current performance of our APGD reactor towards syngas formation in its desired ratio. Figure 6 presents the H_2/CO ratio for different currents (a) and flow rates (b) at a CH_4 fraction of 25%, as well as for different CH_4 fractions at (c) 35 mA & 1 L/min and (d) 25 mA & 0.5 L/min.
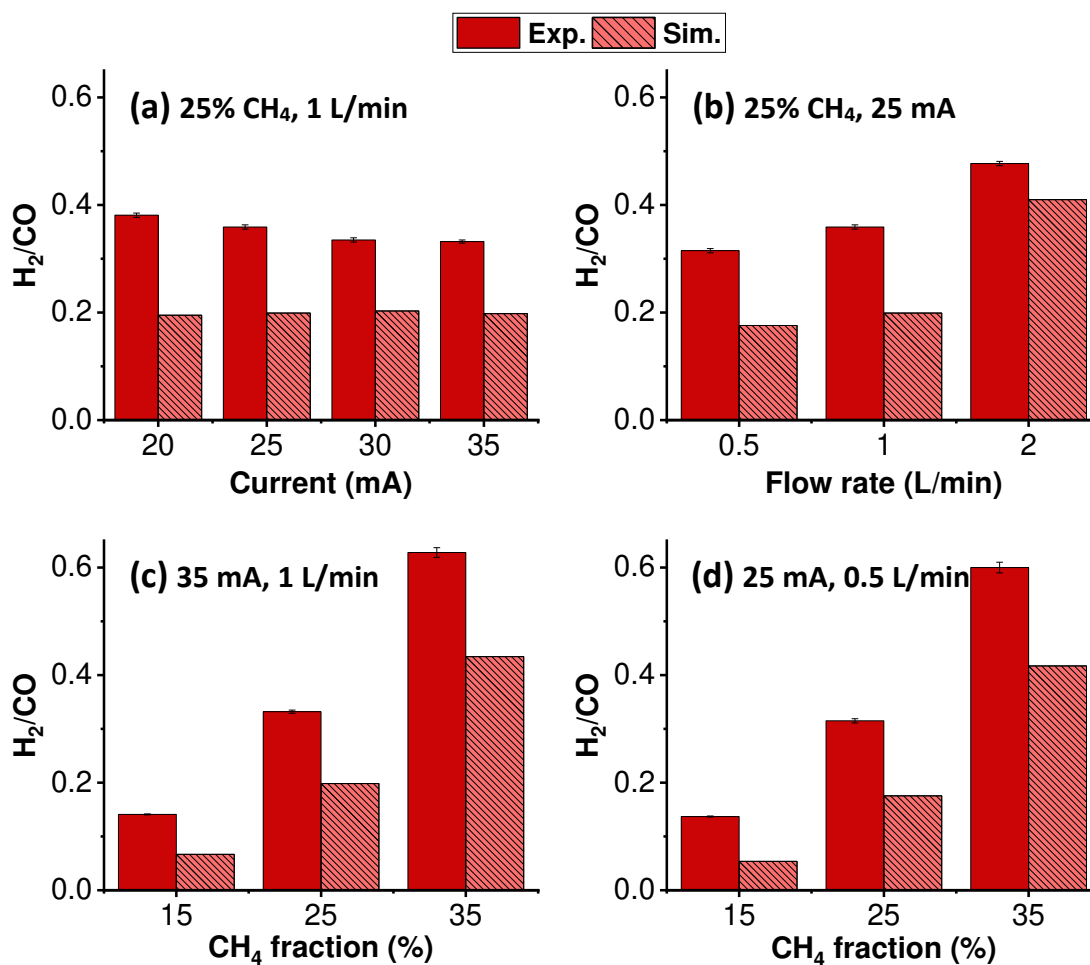
Figure 6: Experimental and simulated syngas ratio as a function of current (a), flow rate (b) and CH_4 fraction (c, d). The other conditions that are kept constant are indicated in the figure. Error bars are added for the experimental results, but are often too small to be visible.

Because we are limited in increasing the CH_4 fraction, we cannot reach the ideal ratio of 2, and even a ratio of 1 is not reached. Indeed, the highest H_2/CO ratio obtained at 35% CH_4 is equal to 0.628 ± 0.009 (a) and 0.60 ± 0.01 (b). This indicates that the current set up, despite the excellent conversion and energy cost obtained, cannot provide a high-value syngas gas stream at this point. Nevertheless, we believe that additional adjustments can be made to both the set up and the process to increase the H_2/CO ratio, and the product output in general. Indeed, it is for example shown in literature that the addition of fractions of oxygen or water, allow for increased amounts of CH_4 in the inlet gas mixture, and therefore a higher H_2/CO ratio[29,37,39]. This is called oxy- and bi-reforming of methane, respectively. Furthermore, it is also shown that a catalyst bed and a second inlet downstream to add additional amounts of CH_4, can increase the H_2/CO ratio above 1[29–31]. Therefore, with the excellent performance of our reactor for DRM in terms of conversion and energy cost demonstrated already at this point, we expect that such adjustments will further improve the reactor's potential. Thus, improving the value of the product output, along these lines, will be the subject of our further research.

In terms of trends, the H_2/CO ratio clearly rises upon higher CH_4 fractions, which is logical, since H_2 can only be formed out of CH_4. For different currents and flow rates the differences are smaller, although there is a clear increase at lower currents and higher flow rates. This is due to the fact that, since CH_4 is more easily converted than CO_2, a lower SEI has a larger negative effect on the CO_2 conversion. For example, at 25 mA & 2 L/min there is almost a factor 2 difference between the CO_2 and CH_4 conversion, and therefore more H_2 is formed relative to CO. Note that the agreement between experiments and

12

model is not so good regarding absolute values, which will be discussed below, but the trends are correctly captured by the model.

Next to syngas, other gasses are formed at all conditions, like C_2H_2, C_2H_4 and C_2H_6, but the sum of their concentrations often doesn't exceed 1%. Among these C_2-components, C_2H_2 is always the most abundant (between 50-90%), followed by C_2H_4 (10-35%) and C_2H_6 (1-10%). In addition, some solid carbon is deposited during the experiments, and although it destabilises the plasma to some extent at 35% CH_4, its overall concentration in the mixture is relatively low, as deduced from the obtained carbon balance, which is always very close to 1. Finally, a liquid fraction is formed, consisting of water and small amounts of oxygenated components. One liquid fraction, collected under the conditions of 25% CH_4, 20 mA and 1 L/min, was analysed by means of GC and HPLC (see details in SI, section 1.1). Next to water, the components that were identified were formaldehyde, acetic acid and methanol, with a concentration of 204 ± 2 ppm, 115 ± 2 ppm and 24 ± 1 ppm, respectively. No other components were detected within the ppm range. This corresponds with other observations throughout literature[5,18,40]. Note that although it was possible to quantify the concentration of these components in the collected liquid fraction, the exact amount is difficult to determine since a lot of liquid product was lost as well, through condensation at the reactor walls or between the reactor and the liquid trap. Therefore, this should be considered to be more a qualitative analysis, in order to determine which oxygenated components are formed and what their relative amounts are. The condition of the liquid sample that was analysed was chosen because of the lower SEI, because based on literature[40] and our quasi-1D model, the concentration of oxygenated components does not rise with higher SEI, nor are any new products formed in significant amounts. In terms of CH_4 fraction, due to the small range investigated, we expect no significant differences in concentration between the different fractions.

A better overview of the quantities of the main products formed can be obtained by looking at the (C-, H- and O-based) selectivities and yields. The selectivity is defined as the amount of atoms a that end up in product j, with respect to the amount of atoms a that are available through conversion of the reactant(s) i:

$$S_{j,a} = \frac{\mu_{j,a} \cdot \alpha \cdot c_j^{out}}{\sum_i \mu_{i,a} \cdot \left(c_i^{in} - \alpha \cdot c_i^{out} \right)} \tag{E6}$$

With $\mu_{i,a}$ and $\mu_{j,a}$ the amount of atoms a in reactant i and product j, respectively. The yield is defined as the actual amount of product j formed with respect to the maximum amount that could be formed theoretically, based on atom a:

$$Y_{j,a} = \frac{\mu_{j,a} \cdot \alpha \cdot c_j^{out}}{\sum_i \mu_{i,a} \cdot c_i^{in}} \tag{E7}$$

The selectivities and yields at 25 mA & 0.5 L/min, and 15% (a), 25% (b) and 35% (c) CH_4, are presented in Figure 7. The results towards selectivity are quite similar for the other currents and flow rates, as illustrated in the SI (section 3.1).
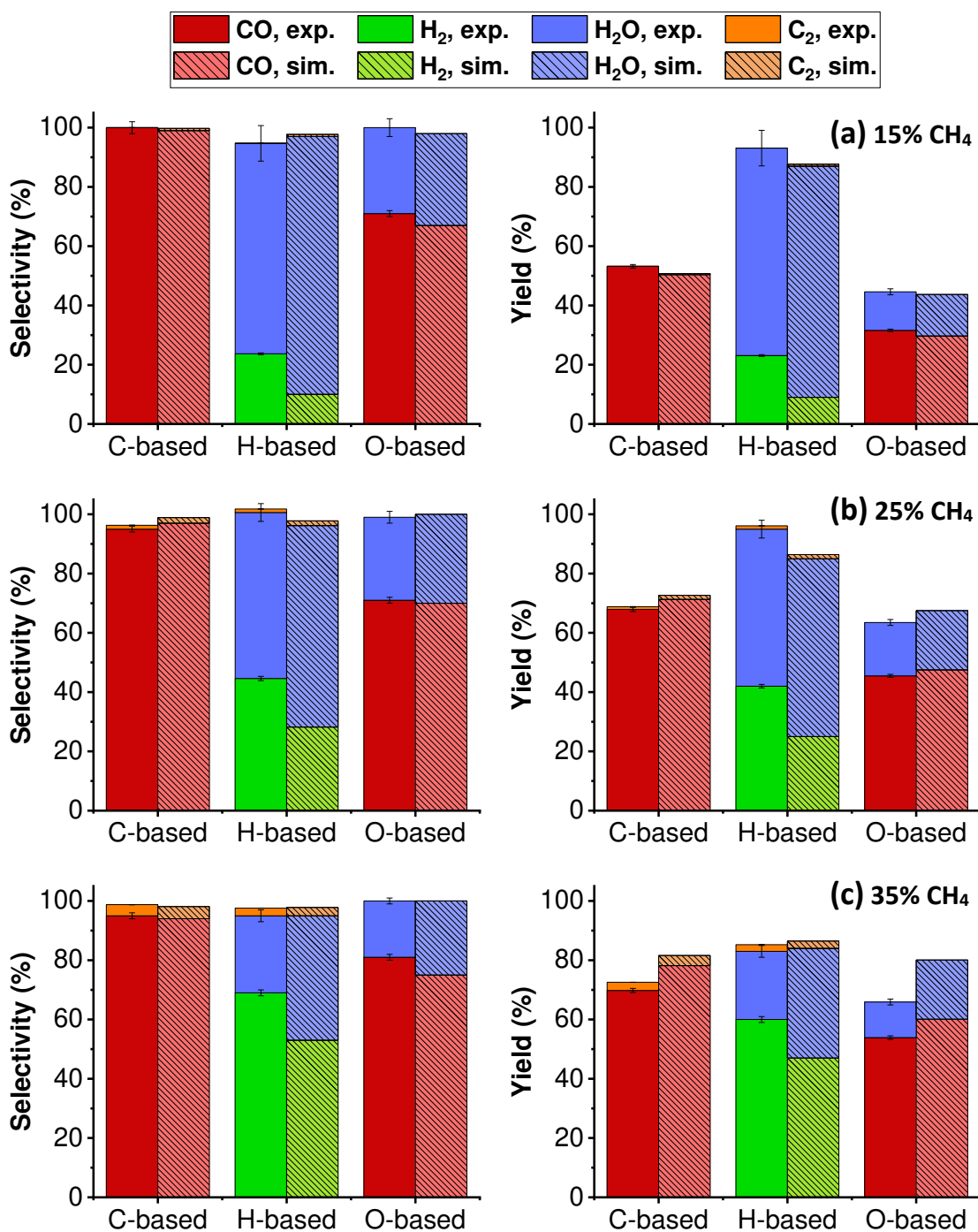
Figure 7: Experimental and simulated C-, H- and O-based selectivities (left) and yields (right) for 15 (a), 25 (b) and 35% (c) CH_4 at 25 mA and 0.5 L/min. C_2H_2, C_2H_4 and C_2H_6 are grouped together as "C_2" but C_2H_2 is the major component (~54 (a), 79 (b) and 86% (c) of the total C_2-fraction). The experimental selectivity and yield for H_2O is calculated based on the approach described by Pinhão et al.[18] (see details in SI, section 1.4). Error bars are added for the experimental results, but are often too small to be visible.

By definition, the sum of all selectivities (being either C-, H- or O-based) should be 100%, when all reaction products are included. Likewise, the sum of all (C-, H- or O-based) yields should be equal to the conversion of the reactants that contain that atom, weighted over the number of atoms and the initial concentration for each reactant. Both are indeed the case in our measurements, as the sum of all selectivities is always very close to 100% and the sum of all yields is always very close to the CO_2, CH_4 or total conversion (in case of O-, H- and C-based yields, respectively). As H_2O could not be

14

measured with our GC, its selectivity and yield was determined following the procedure described by Pinhão et al.[18]; see detailed explanation in the SI (section 1.4). As a consequence of this method, the error bars for H_2O are larger than for the other components, which were measured directly.

The C-based selectivity towards CO is very high for all conditions, in the range of 95-100% for all CH_4 fractions. The C_2-components reach a maximum selectivity of 3.75 ± 0.04 % at 35% CH_4, and are not visible in Figure 7 at 15% CH_4 (< 0.02%). From the H-based selectivities, we see that either H_2O or H_2 has the highest value. Upon increasing the CH_4 fraction, the H_2O selectivity drops from 71 ± 6 % to 26 ± 2 %, while the H_2 selectivity rises from 23.7 ± 0.3 % to 69 ± 1 %. The H-based selectivity for the C_2-components is similar as observed for the C-based selectivities (i.e. < 3%), with again a small increase towards higher CH_4 fractions. Finally, the O-based selectivity towards CO is always in the range of 70-80%, with the highest value at 35% CH_4, while the remaining fraction is mostly H_2O (see above). It should be mentioned that a very small fraction of O_2 was also detected during experiments, but due to its too low concentration at all conditions it was not plotted in Figure 7.

The same relative differences are observed for the yields, as these are equal to the product of selectivity and conversion. Note that the highest yield for syngas is obtained at 35% CH_4, due to the higher selectivity for H_2 over H_2O at higher CH_4 fraction. Figure 7 also confirms the rising trend in H_2/CO ratio observed in Figure 6, as the H_2 yield strongly increases for higher CH_4 fractions, while the CO yield does not rise to the same extent. When comparing all different currents and flow rates (see SI; section 3.1), the selectivities remain relatively constant, but as a general trend, the C_2-components become somewhat more important upon lower SEI, although their C- and H-based selectivity is never above 5 and 4.5%, respectively.

The same trends are observed for both the experiments and simulations, although the selectivity for H_2 seems to be systematically underestimated by the model. Simultaneously, a systematic overestimation of the selectivity for H_2O and C_2-components is observed as well. Because this is observed across all conditions (see SI, section 3.1), this deviation is most likely due to some reactions in the chemistry set of which the rate coefficients are under- or overestimated. Indeed, some of these values in literature are subject to uncertainties, but we prefer not to tune these rate coefficients in order to reach better agreement without physical basis. Note that this explains why in Figure 6, the experimental and simulated H_2/CO ratios deviate significantly in terms of absolute values as well.

As far as the yields are concerned, because they are related to both conversion and selectivity, their deviation between experimental and simulated values is overall somewhat larger, especially at 35% CH_4, due to the somewhat larger deviation in conversion in this case. In general, however, the agreement between experiments and simulations is quite reasonable, which indicates that the model provides a realistic picture of the plasma chemistry, and can be used for analysing the reaction paths, as explained in next section.

3.5. Reaction pathway analysis

Figure 8 illustrates the most important reaction paths from CO_2 and CH_4, towards and in between the experimentally detected components, obtained from the model based on the calculated rates at the end of the plasma reactor. The figure shows the results at 25% CH_4, 30 mA and 1 L/min, which is in the middle of the range of conditions measured, both regarding CH_4 fraction and SEI, so it is best suited to discuss the overall plasma chemistry taking place during our experiments. In fact, the differences between the different conditions are very small, so the main conclusions are valid for the entire range of conditions. Not all reactions are shown in this overview, as a lot of reactions only proceed at a very small rate, and including them would not contribute to a better understanding of the overall chemistry.

The densities of the main plasma species important to the overall chemistry are plotted as a function of position in the plasma in Figure 9, for the same conditions as in Figure 8.
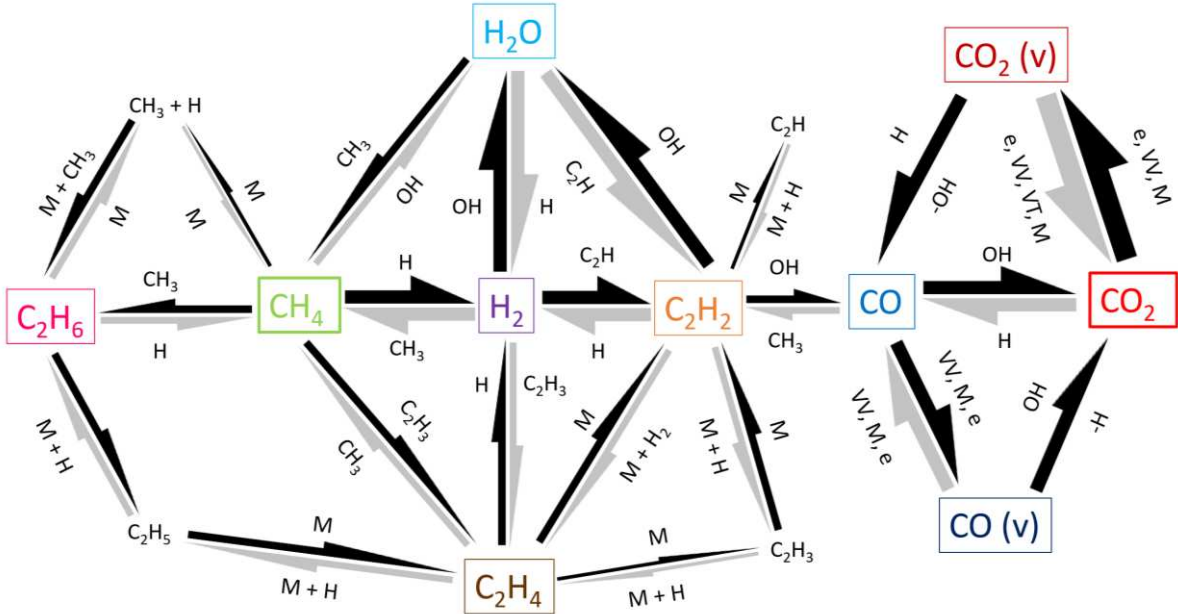
Figure 8: Reaction scheme revealed by the model, based on the most important reactions for 25% CH_4, 30 mA and 1 L/min. The experimentally detected molecules, as well as the vibrationally excited states, are framed and coloured. M stands for any neutral molecule. Black arrows represent the dominant direction of the reaction, and species next to the arrows are the reactants for these reactions. The thickest arrows represent a reaction rate in the order of 10^{21} cm^{-3} s^{-1}, while the thinnest arrows represent a reaction rate in the order of 10^{18} cm^{-3} s^{-1}.
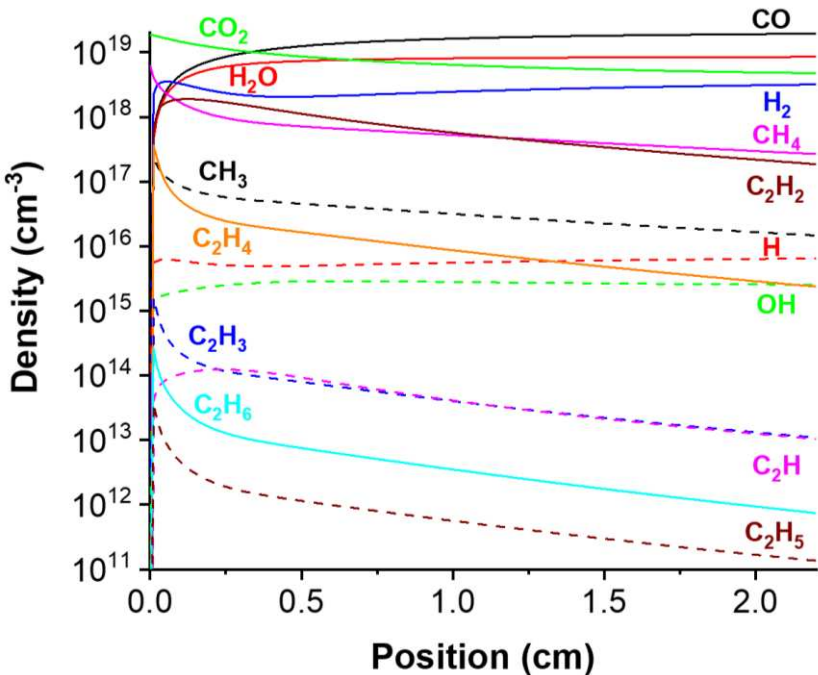
Figure 9: Calculated densities as a function of position in the plasma, for all experimentally detected molecules (solid lines) and important radicals (dashed lines), at 25% CH_4, 30 mA and 1 L/min.

(a) Main CO_2 and CH_4 conversion pathways

A steady but clear drop in density for both CO_2 and CH_4 is observed in Figure 9, being most pronounced for CH_4, confirming our experimental observations of the higher CH_4 conversion. Figure 8 indicates that

the most important mechanism for CO_2 conversion is the reaction with a H atom, after vibrational excitation of CO_2, leading to CO and an OH radical:

$$CO_2(v) + H \rightleftharpoons CO + OH \hspace{5cm} (R2)$$

The reverse reaction is the most important formation reaction of CO_2, either directly from CO in its ground state or after vibrational excitation of CO. However, the equilibrium clearly points towards CO, because of the high concentration and the favoured conditions for vibrationally excited CO_2. Indeed, the reduced electric field in the APGD is in the order of 50 Td (1 Td = 10^{-21} V m^2), similar as for other warm plasmas (like GA and MW plasmas), where most of the electron energy goes into vibrational excitation.[5] The vibrational distribution function (VDF) of CO_2 at the same conditions as Figure 8 and 9 is plotted in the SI (section 3.2). It follows a Boltzmann distribution, indicating that the VDF is rather thermal, in equilibrium with the gas temperature, which is also in line with other warm plasmas[5–8,14,23], but due to the relatively high gas temperature of 2000-3000 K, the (lowest) vibrational levels have a considerable population density, explaining their importance in the CO_2 conversion.

The H atoms used for CO_2 splitting (in R2) are initially coming from the reaction of CH_4 with any neutral molecule:

$$CH_4 + M \rightleftharpoons CH_3 + H + M \hspace{5cm} (R3)$$

After this initial reaction, H atoms are both formed and consumed in a large number of reactions in Figure 8. Because of reactions (R2) and (R3), the CO_2 conversion rises upon a higher CH_4 fraction, as seen in Figure 3.

As soon as CH_4 splitting has started (by R3), the produced H atoms lead to further conversion of CH_4 into H_2:

$$CH_4 + H \rightleftharpoons H_2 + CH_3 \hspace{5cm} (R4)$$

The main formation mechanism of CH_4 is the reaction of H_2O with CH_3 radicals:

$$H_2O + CH_3 \rightleftharpoons CH_4 + OH \hspace{5cm} (R5)$$

Note that the dominant direction towards CH_4 is due to the relatively high density of H_2O towards the end of the plasma reactor, as seen in Figure 9. Earlier in the plasma, i.e., in the first few mm's, reaction (R5) proceeds in the direction of H_2O, with the second highest rate of all reactions involving CH_4, and this explains the (initial) formation of H_2O (see fast rise in density in the first few mm's in Figure 9). Figure 3 illustrated that the CH_4 conversion drops upon rising CH_4 fraction. This is due to a drop in OH density in the mixture (produced by (R2), which becomes less important at lower CO_2 fraction), leading to a shift of reaction (R5) towards the right, explaining the lower (net) conversion of CH_4.

(b) Pathways to the main reaction products

The dominance of reactions (R2) and (R4) explains why syngas is the main reaction product. The rise in H_2/CO ratio for higher CH_4/CO_2 ratios is also very clear through reactions (R2) and (R4). Figure 9 indicates a clear rise in CO density as a function of distance in the plasma, while the H_2 density exhibits an initial rise, followed by a slight drop till ca. 0.75 cm, after which it slightly rises towards the end. This drop is attributed to the high concentrations of OH and C_2H radicals, which convert H_2 into H_2O and C_2H_2, respectively, as illustrated in Figure 8. The rise towards the end is due to a stabilisation of the OH density and a drop in the C_2H density.

Figure 9 also shows that the H_2O density continues to rise over the entire plasma reactor length. The two main formation mechanisms by the end of the plasma reactor are the reactions of an OH radical with H_2 or C_2H_2 (cf. Figure 8):

$$H_2 + OH \rightleftharpoons H_2O + H \qquad (R6)$$

$$C_2H_2 + OH \rightleftharpoons H_2O + C_2H \qquad (R7)$$

Note that the direct formation of H_2O out of C_2H_4 (through OH radicals) is also possible, however the stepwise formation through H_2 is much more important, hence the direct reaction is not explicitly shown in Figure 8.

The fact that these reactions are so important is not beneficial, as the formation of H_2O over H_2 is an economic loss. Experimentally, we observed that a higher CH_4 fraction leads to a higher H_2 concentration and a lower H_2O concentration. Indeed, a higher CH_4 concentration and a lower CO_2 concentration will shift the equilibrium of (R3) to the right and of (R2) to the left, respectively, yielding a higher H/OH ratio. This shifts the equilibrium of (R6) in the direction of H_2, hence promoting its formation, while the formation of H_2O is suppressed.

The C_2-components are initially formed through CH_3 radicals, originating from reactions (R3), (R4) and (R5 – reverse direction), which recombine into C_2H_6 (R8). Upon rising CH_4 fraction, the concentration of C_2 components rises as well, as observed in our experiments. Figure 8 illustrates that C_2H_6 easily reacts further into C_2H_5 radicals (R9), which further react to C_2H_4 (R10):

$$CH_3 + CH_3 + M \rightleftharpoons C_2H_6 + M \qquad (R8)$$

$$C_2H_6 \rightleftharpoons C_2H_5 + H \qquad (R9)$$

$$C_2H_5 + M \rightleftharpoons C_2H_4 + H + M \qquad (R10)$$

A similar reaction pathway occurs for the formation of C_2H_2 out of C_2H_4, which explains why C_2H_2 has the highest density of all C_2-components and C_2H_6 the lowest (see Figure 9). This happens almost immediately in the beginning of the plasma reactor. Towards the end, C_2H_2 is also easily formed directly out of C_2H_4 upon reaction with any neutral molecule (R11), and from H_2 upon reaction with C_2H radicals formed earlier in the plasma (R12):

$$C_2H_4 + M \rightleftharpoons C_2H_2 + H_2 + M \qquad (R11)$$

$$H_2 + C_2H \rightleftharpoons C_2H_2 + H \qquad (R12)$$

Note that the direct formation of C_2H_2 from CH_4 is also possible, upon reaction with C_2H radicals. However, just as for the direct formation of H_2O out of C_2H_4, the overall rate for the stepwise formation of C_2H_2 through H_2 is significantly larger than the direct formation, hence this reaction is not explicitly shown in Figure 8.

The main conversion pathways for C_2H_2 are through reactions with OH radicals to form H_2O (R7), but also CO (R13):

$$C_2H_2 + OH \rightleftharpoons CO + CH_3 \qquad (R13)$$

As the carbon atoms in the C_2-components primarily originate from CH_4 through the CH_3 radicals (R8), the very high C-based selectivity for CO in Figure 7, even at 35% CH_4, can be explained through reaction (R13), which provides a pathway for the carbon atoms originating from CH_4 into CO. Furthermore, it explains why the selectivity of CO drops for a lower CO_2/CH_4 ratio, as there is a lower production rate

of OH radicals (R2) and higher production rate of CH_3 radicals (R3, R4, R5 – reverse direction), shifting the equilibrium of (R13) in the direction of C_2H_2.

Finally, Figure 9 indicates that the density for all C_2-components constantly decreases, after reaching a maximum very early in the plasma reactor. Based on Figure 8, this means that from a certain distance, when also the CO_2 and CH_4 conversion starts to reach some steady-state, the equilibrium is shifted away from the C_2-components in favour of H_2, CO and H_2O as products. This explains why in our experiments a higher SEI (leading to an earlier steady state) gives a slightly lower selectivity and yield for these C_2-components.

4. Conclusion

We investigated the performance of a confined APGD plasma reactor for DRM, reaching a total conversion up to 74%. The energy cost generally stays below 4.27 eV/molecule, which is the efficiency target defined by Snoeckx and Bogaerts, for plasma-based DRM to be competitive with classical DRM and other emerging technologies[5]. This performance is among the best compared to the current state-of-the-art for plasma-based DRM for all types of plasma reactors reported in literature, demonstrating the importance of confining the reactor to the size of the plasma width. CO and H_2 are the major products, followed by H_2O and C_2H_2.

We also developed a quasi-1D chemical kinetics model, showing good agreement with the experiments. A reaction pathway analysis reveals that the CO_2 conversion is largely initiated by vibrational excitation of CO_2. Furthermore, the H atoms are found to be very important for both CO_2 and CH_4 conversion, while a large concentration of OH radicals is detrimental, as it promotes H_2O above H_2 formation, and the recombination with CO, yielding again CO_2, hence reducing the net CO_2 conversion.

Our experiments were limited to a CH_4 fraction up to 35%, because higher CH_4 fractions gave rise to unstable plasma, due to carbon formation. Further research will focus on alternative routes for achieving a higher H_2/CO ratio, while avoiding carbon formation, to achieve a more valuable product output with our confined APGD plasma reactor.

Acknowledgements

References

(1)   Kathiraser, Y.; Oemar, U.; Saw, E. T.; Li, Z.; Kawi, S. Kinetic and Mechanistic Aspects for CO2 Reforming of Methane over Ni Based Catalysts. *Chem. Eng. J.* **2015**, *278*, 62–78. https://doi.org/10.1016/j.cej.2014.11.143.

(2)   Lu, W.; Cao, Q.; Xu, B.; Adidharma, H.; Gasem, K.; Argyle, M.; Zhang, F.; Zhang, Y.; Fan, M. A New Approach of Reduction of Carbon Dioxide Emission and Optimal Use of Carbon and Hydrogen Content for the Desired Syngas Production from Coal. *J. Clean. Prod.* **2020**, *265*,

121786. https://doi.org/10.1016/j.jclepro.2020.121786.

(3)   Zhou, L. M.; Xue, B.; Kogelschatz, U.; Eliasson, B. Nonequilibrium Plasma Reforming of Greenhouse Gases to Synthesis Gas. *Energy and Fuels* **1998**, *12* (6), 1191–1199. https://doi.org/10.1021/ef980044h.

(4)   Mehariya, S.; Iovine, A.; Casella, P.; Musmarra, D.; Figoli, A.; Marino, T.; Sharma, N.; Molino, A. *Fischer-Tropsch Synthesis of Syngas to Liquid Hydrocarbons*; INC, 2019. https://doi.org/10.1016/B978-0-12-815936-1.00007-1.

(5)   Snoeckx, R.; Bogaerts, A. Plasma Technology-a Novel Solution for CO2 Conversion? *Chem. Soc. Rev.* **2017**, *46* (19), 5805–5863. https://doi.org/10.1039/c6cs00066e.

(6)   Bogaerts, A.; Neyts, E. C. Plasma Technology: An Emerging Technology for Energy Storage. *ACS Energy Lett.* **2018**, *3* (4), 1013–1027. https://doi.org/10.1021/acsenergylett.8b00184.

(7)   Cleiren, E.; Heijkers, S.; Ramakers, M.; Bogaerts, A. Cover Feature: Dry Reforming of Methane in a Gliding Arc Plasmatron: Towards a Better Understanding of the Plasma Chemistry (ChemSusChem 20/2017). *ChemSusChem* **2017**, *10* (20), 3864–3864. https://doi.org/10.1002/cssc.201701891.

(8)   Slaets, J.; Aghaei, M.; Ceulemans, S.; Van Alphen, S.; Bogaerts, A. CO2 and CH4 Conversion in "Real" Gas Mixtures in a Gliding Arc Plasmatron: How Do N2 and O2 Affect the Performance? *Green Chem.* **2020**, *22* (4), 1366–1377. https://doi.org/10.1039/c9gc03743h.

(9)   Abiev, R. S.; Sladkovskiy, D. A.; Semikin, K. V.; Murzin, D. Y.; Rebrov, E. V. Non-Thermal Plasma for Process and Energy Intensification in Dry Reforming of Methane. *Catalysts* **2020**, *10* (11), 1–41. https://doi.org/10.3390/catal10111358.

(10)   Allah, Z. A.; Whitehead, J. C. Plasma-Catalytic Dry Reforming of Methane in an Atmospheric Pressure AC Gliding Arc Discharge. *Catal. Today* **2015**, *256* (P1), 76–79. https://doi.org/10.1016/j.cattod.2015.03.040.

(11)   Lu, N.; Sun, D.; Xia, Y.; Shang, K.; Wang, B.; Jiang, N.; Li, J.; Wu, Y. Dry Reforming of CH4–CO2 in AC Rotating Gliding Arc Discharge: Effect of Electrode Structure and Gas Parameters. *Int. J. Hydrogen Energy* **2018**, *43* (29), 13098–13109. https://doi.org/10.1016/j.ijhydene.2018.05.053.

(12)   Chung, W. C.; Chang, M. B. Dry Reforming of Methane by Combined Spark Discharge with a Ferroelectric. *Energy Convers. Manag.* **2016**, *124*, 305–314. https://doi.org/10.1016/j.enconman.2016.07.023.

(13)   Li, D.; Li, X.; Bai, M.; Tao, X.; Shang, S.; Dai, X.; Yin, Y. CO2 Reforming of CH4 by Atmospheric Pressure Glow Discharge Plasma: A High Conversion Ability. *Int. J. Hydrogen Energy* **2009**, *34* (1), 308–313. https://doi.org/10.1016/j.ijhydene.2008.10.053.

(14)   Trenchev, G.; Nikiforov, A.; Wang, W.; Kolev, S.; Bogaerts, A. Atmospheric Pressure Glow Discharge for CO2 Conversion: Model-Based Exploration of the Optimum Reactor Configuration. *Chem. Eng. J.* **2019**, *362* (December 2018), 830–841. https://doi.org/10.1016/j.cej.2019.01.091.

(15)   Huang, A.; Xia, G.; Wang, J.; Suib, S. L.; Hayashi, Y.; Matsumoto, H. CO2 Reforming of CH4 by Atmospheric Pressure Ac Discharge Plasmas. *J. Catal.* **2000**, *189* (2), 349–359. https://doi.org/10.1006/jcat.1999.2684.

(16)   Yang, Y. Methane Conversion and Reforming by Nonthermal Plasma on Pins. *Ind. Eng. Chem. Res.* **2002**, *41* (24), 5918–5926. https://doi.org/10.1021/ie0202322.

(17) Chen, Q.; Dai, W.; Tao, X.; Yu, H.; Dai, X.; Yin, Y. CO2 Reforming of CH4 by Atmospheric Pressure Abnormal Glow Plasma. *Plasma Sci. Technol.* **2006**, *8* (2), 181–184. https://doi.org/10.1088/1009-0630/8/2/12.

(18) Pinhão, N.; Moura, A.; Branco, J. B.; Neves, J. Influence of Gas Expansion on Process Parameters in Non-Thermal Plasma Plug-Flow Reactors: A Study Applied to Dry Reforming of Methane. *Int. J. Hydrogen Energy* **2016**, *41* (22), 9245–9255. https://doi.org/10.1016/j.ijhydene.2016.04.148.

(19) Pancheshnyi, S.; Eismann, B.; Hagelaar, G. J. M.; Pitchford, L. C. Computer Code ZDPlasKin. http://www.zdplaskin.laplace.univ-tlse.fr/ (University of Toulouse, LAPLACE, CNRS-UPS-INP, Toulouse, France, 2008).

(20) Manion, J. A.; Huie, R. E.; Levin, R. D.; Jr., D. R. B.; Orkin, V. L.; Tsang, W.; McGivern, W. S.; Hudgens, J. W.; Knyazev, V. D.; Atkinson, D. B.; Chai, E.; Tereza, A. M.; Lin, C.-Y.; Allison, T. C.; Mallard, W. G.; Westley, F.; Herron, J. T.; Hampson, R. F.; Frizzell, D. H. NIST Chemical Kinetics Database, NIST Standard Reference Database 17, Version 7.0 (Web Version), Release 1.6.8, Data version 2015.09, National Institute of Standards and Technology, Gaithersburg, Maryland, 20899-8320. https://kinetics.nist.gov/ (accessed Jun 24, 2021).

(21) Hagelaar, G. J. M.; Pitchford, L. C. Solving the Boltzmann Equation to Obtain Electron Transport Coefficients and Rate Coefficients for Fluid Models. *Plasma Sources Sci. Technol.* **2005**, *14* (4), 722–733. https://doi.org/10.1088/0963-0252/14/4/011.

(22) Heijkers, S. Plasma Chemistry Modelling for CO2 and CH4 Conversion in Various Plasma Types, University of Antwerp, 2020.

(23) Ramakers, M.; Trenchev, G.; Heijkers, S.; Wang, W.; Bogaerts, A. Gliding Arc Plasmatron: Providing an Alternative Method for Carbon Dioxide Conversion. *ChemSusChem* **2017**, *10* (12), 2642–2652. https://doi.org/10.1002/cssc.201700589.

(24) Dinh, D. K.; Trenchev, G.; Lee, D. H.; Bogaerts, A. Arc Plasma Reactor Modification for Enhancing Performance of Dry Reforming of Methane. *J. CO2 Util.* **2020**, *42*, 101352. https://doi.org/10.1016/j.jcou.2020.101352.

(25) Li, L.; Zhang, H.; Li, X.; Kong, X.; Xu, R.; Tay, K.; Tu, X. Plasma-Assisted CO 2 Conversion in a Gliding Arc Discharge: Improving Performance by Optimizing the Reactor Design. *J. CO2 Util.* **2019**, *29*, 296–303. https://doi.org/10.1016/j.jcou.2018.12.019.

(26) Jahn, R. G.; Lyman, F. A. Physics of Electric Propulsion. *Journal of Applied Mechanics*. 1969, pp 117–118. https://doi.org/10.1115/1.3564751.

(27) Mancinelli, B.; Prevosto, L.; Chamorro, J. C.; Minotti, F. O.; Kelly, H. Modelling of the Plasma–Sheath Boundary Region in Wall-Stabilized Arc Plasmas: Unipolar Discharge Properties. *Plasma Chem. Plasma Process.* **2018**, *38* (1), 147–176. https://doi.org/10.1007/s11090-017-9859-x.

(28) Andersen, J. A.; Christensen, J. M.; Østberg, M.; Bogaerts, A.; Jensen, A. D. Plasma-Catalytic Dry Reforming of Methane: Screening of Catalytic Materials in a Coaxial Packed-Bed DBD Reactor. *Chem. Eng. J.* **2020**, *397*, 125519. https://doi.org/10.1016/j.cej.2020.125519.

(29) Li, K.; Liu, J. L.; Li, X. S.; Lian, H. Y.; Zhu, X.; Bogaerts, A.; Zhu, A. M. Novel Power-to-Syngas Concept for Plasma Catalytic Reforming Coupled with Water Electrolysis. *Chem. Eng. J.* **2018**, *353* (July), 297–304. https://doi.org/10.1016/j.cej.2018.07.111.

(30) Li, K.; Liu, J. L.; Li, X. S.; Zhu, X.; Zhu, A. M. Warm Plasma Catalytic Reforming of Biogas in a Heat-Insulated Reactor: Dramatic Energy Efficiency and Catalyst Auto-Reduction. *Chem. Eng.*

J. **2016**, *288*, 671–679. https://doi.org/10.1016/J.CEJ.2015.12.036.

(31)   Li, K.; Liu, J. L.; Li, X. S.; Zhu, X. B.; Zhu, A. M. Post-Plasma Catalytic Oxidative CO2 Reforming of Methane over Ni-Based Catalysts. *Catal. Today* **2015**, *256* (P1), 96–101. https://doi.org/10.1016/j.cattod.2015.03.013.

(32)   Xia, Y.; Lu, N.; Li, J.; Jiang, N.; Shang, K.; Wu, Y. Combined Steam and CO2 Reforming of CH4 for Syngas Production in a Gliding Arc Discharge Plasma. *J. CO2 Util.* **2020**, *37*, 248–259. https://doi.org/10.1016/J.JCOU.2019.12.016.

(33)   Sun, H.; Lee, J.; Bak, M. S. Experiments and Modeling of Atmospheric Pressure Microwave Plasma Reforming of a Methane-Carbon Dioxide Mixture. *J. CO2 Util.* **2021**, *46*, 101464. https://doi.org/10.1016/j.jcou.2021.101464.

(34)   Montesano, C.; Faedda, M.; Martini, L. M.; Dilecce, G.; Tosi, P. CH4reforming with CO2in a Nanosecond Pulsed Discharge. The Importance of the Pulse Sequence. *J. CO2 Util.* **2021**, *49*, 101556. https://doi.org/10.1016/j.jcou.2021.101556.

(35)   Chun, S. M.; Hong, Y. C.; Choi, D. H. Reforming of Methane to Syngas in a Microwave Plasma Torch at Atmospheric Pressure. *J. CO2 Util.* **2017**, *19*, 221–229. https://doi.org/10.1016/j.jcou.2017.03.016.

(36)   Lašič Jurković, D.; Liu, J. L.; Pohar, A.; Likozar, B. Methane Dry Reforming over Ni/Al2O3 Catalyst in Spark Plasma Reactor: Linking Computational Fluid Dynamics (CFD) with Reaction Kinetic Modelling. *Catal. Today* **2021**, *362* (December 2019), 11–21. https://doi.org/10.1016/j.cattod.2020.05.028.

(37)   Majd Alawi, N.; Hung Pham, G.; Barifcani, A.; Hoang Nguyen, M.; Liu, S. Syngas Formation by Dry and Steam Reforming of Methane Using Microwave Plasma Technology. *IOP Conf. Ser. Mater. Sci. Eng.* **2019**, *579* (1). https://doi.org/10.1088/1757-899X/579/1/012022.

(38)   Spath, P. L.; Dayton, D. C. Preliminary Screening -- Technical and Economic Assessment of Synthesis Gas to Fuels and Chemicals with Emphasis on the Potential for Biomass-Derived Syngas. *Natl. Renew. Energy Lab.* **2003**, No. December, 1–160. https://doi.org/10.2172/15006100.

(39)   Snoeckx, R.; Wang, W.; Zhang, X.; Cha, M. S.; Bogaerts, A. Plasma-Based Multi-Reforming for Gas-To-Liquid: Tuning the Plasma Chemistry towards Methanol. *Sci. Rep.* **2018**, *8* (1), 1–7. https://doi.org/10.1038/s41598-018-34359-x.

(40)   Krawczyk, K.; Młotek, M.; Ulejczyk, B.; Schmidt-Szałowski, K. Methane Conversion with Carbon Dioxide in Plasma-Catalytic System. *Fuel* **2014**, *117* (PART A), 608–617. https://doi.org/10.1016/J.FUEL.2013.08.068.